## RESEARCH LETTER

**Key Points:**
- We quantify lunar surface roughness using high-resolution optical images and topography and model the stability of near-surface water ice
- Surface roughness in regions where surface water ice is predicted to be thermally stable is lower than in warmer areas
- Cold-trapping of ice or enhanced ice-rich regolith transport may lead to the reduced small-scale topographic roughness

**Supporting Information:**
- Supporting Information S1

**Correspondence to:**
S. Moon,
sgmoon@ucla.edu

# Geomorphic Evidence for the Presence of Ice Deposits in the Permanently Shadowed Regions of Scott-E Crater on the Moon

**Seulgi Moon[1]** , **David A Paige[1]** , **Matthew A Siegler[2]** , and **Patrick S Russell[1]**

[1]Earth, Planetary, and Space Sciences, University of California, Los Angeles, CA, USA, [2]Planetary Science Institute, Dallas, TX, USA

**Abstract** The abundance and distribution of ice on the Moon are still unknown. Here, we examine the connections between geomorphic characteristics and the potential presence of lunar ice in permanently shadowed regions of the Scott-E crater in the lunar south polar region. We first quantify surface characteristics, such as roughness, based on high-resolution optical images and topography data and then model spatial variations of water ice stability using a high-resolution thermal model. We find that the surface roughness in regions where thermally stable surface ice is predicted is significantly lower than in adjacent regions where subsurface ice or no ice is predicted. This correspondence may result from processes such as preferential cold-trapping in depressions or high albedo areas, or enhanced regolith transport in the ice-rich regolith.

**Plain Language Summary** Permanently shadowed regions (PSRs) near the lunar north and south poles are never exposed to direct sunlight. As a result, these regions have extremely low temperatures and have a high potential for hosting water ice on the surface or in the shallow subsurface. However, few studies have shown unequivocal evidence for the presence of lunar ice deposits in PSRs. In this study, we examine whether surface or subsurface ice may cause measurable changes in surface characteristics of the Moon. To show this, we quantify the spatial variation of surface roughness and model ice stability on the surface and subsurface in a PSR in the lunar south polar region. We find that areas where thermal models predict stable surface ice tend to have subdued surface roughness variations. This may be caused by enhanced transport of ice-rich surface material or preferential trapping of ice in local low-elevation areas or high albedo areas.

## 1. Introduction

The first-order controls of the abundance and distribution of ice on the Moon are not well known. Unlike Mercury (Harmon, 2008), the Moon does not possess extensive radar-bright areas of pure ice in its permanently shadowed regions (PSRs) (Campbell et al., 2003). However, evidence from the Lunar Crater Observation and Sensing Satellite (LCROSS) mission (Colaprete et al., 2010), Lunar Orbiter Laser Altimeter (LOLA) (Fisher et al., 2017; Zuber et al., 2012), Lyman Alpha Mapping Project instruments (Hayne et al., 2015) on the Lunar Reconnaissance Orbiter (LRO), and the Moon Mineralogy Mapper ($M^3$) instrument (Li et al., 2018) suggest that there are patchy ice deposits in low concentrations exposed on the surface. The extent to which these surface ice deposits are related to possibly more extensive deposits of deeper ice is currently unknown (Lawrence, 2017).

A few studies have applied techniques from geomorphic analysis to address the question of lunar ice (Deutsch et al., 2020; Rubanenko et al., 2019). On Earth and other solar system bodies, quantitative landform analysis has proven valuable for identifying the presence of near-surface ice deposits or ice-rich surface materials (Boeckli et al., 2012; Kreslavsky & Head, 2000; Mangold, 2003; Mahaney et al., 2007; Rossbacher & Judson, 1981). Recently, Rubanenko et al. (2019) published a statistical survey of the depth-to-diameter ratios of small (2–15 km) diameter craters in the polar regions of Mercury and the Moon and found that these craters become distinctly shallower near the north pole of Mercury and the south pole of the Moon. They attribute the observed shallowing to the presence of abundant buried water ice deposits (up to tens of meters thick) intermixed with regolith. Furthermore, the locations of shallow polar craters on the moon are statistically correlated with the locations of previously detected surface ice deposits from the $M^3$ instrument,

suggesting that some of this subsurface ice is being exhumed or linked to the surface via diffusion (Rubanenko et al., 2019).

Spatial distribution of topographic metrics, such as surface roughness, a measure of surface elevation or texture changes, and their scale dependency has been related to surface material properties or landscape formation mechanisms of planetary surfaces (Calef et al., 2014; Kim & Muller, 2008; Kreslavsky et al., 2013; Rosenburg et al., 2011). For example, Kreslavsky et al., (2013) quantified the topographic roughness of the Moon at the 100s meter- and kilometer-scales and found that the spatial distributions of these roughness values are different from each other. They attribute the 100s meter-scale roughness to regolith accumulation and modification processes such as primary impacts and secondary ejectors. Kilometer-scale roughness is attributed to geological processes such as large-scale impacts, volcanism, and tectonics.

Variations of topographic roughness have been related to the presence of ice in the regolith of Mars (Chamberlain & Boynton, 2007; Kreslavsky & Head, 2000; Mustard et al., 2001) and Mercury (Chabot et al., 2016). Kreslavsky and Head (2000) found a systematic decrease in km-scale topographic roughness with several meters of vertical relief differences toward high latitudes on Mars. The authors attributed these changes of topographic roughness to the presence of smoothing mantles in regolith that are potentially affected by seasonal frost, subsurface ice, climatic conditions (temperature, humidity), and global wind patterns. In addition, geomorphic features, such as lobate debris aprons, crater fill, and terrain softening, on Mars have been related to ground ice through processes like viscous creep (Chamberlain & Boynton, 2007; Mustard et al., 2001; Squyres & Carr, 1986).

High-resolution imaging of the PSRs in high-latitude craters on Mercury via scattered sunlight has revealed the presence of dark surface deposits as well as the presence of exposed surface ice (Chabot et al., 2016). However, analogous scattered-light images of PSRs in high-latitude craters on the Moon by the LRO Lunar Reconnaissance Orbiter Camera (LROC) (Cisneros et al., 2018) have thus far failed to reveal analogous features with varying reflectances. Nonetheless, these high-resolution scattered-light images provide information on brightness or illumination variations associated with surface texture or elevation changes that can be related to the presence of lunar ice deposits.

In this study, we examine the connections between geomorphic characteristics and the model-predicted presence of thermally stable surface and subsurface ice in the PSR within Scott-E crater in the south polar region of the Moon. To do this, we first quantify the surface roughness based on high-resolution optical images and topography data. Then, we model the spatial variations of water ice stability using a high-resolution thermal model. Next, by comparing the quantified surface characteristics with thermal model results, we present new results showing the relationships between surface roughness and the modeled distribution of thermally stable surface and subsurface ice. Finally, we discuss potential mechanisms that explain our observations.

## 2. Materials and Methods

### 2.1. Scott-E Crater

Scott-E (Figure 1a) is a 28 km diameter crater centered at 81.2°S, 35.7°E on the lunar nearside (Salamunić-car et al., 2014). Scott-E is located in the northwestern region of the nearby Scott crater centered at 82.3°S, 48.5°E with a diameter of 103 km. While the rim of Scott has been heavily eroded with an estimated age of Pre-Nectarian, the rim of Scott-E is sharp-edged and well-defined with an estimated age of Imbrian (Fortezzo et al., 2020). We chose this crater because of its large size, symmetric circular form, strongly asymmetric north-south illumination, thermal environment, availability of high-quality LROC Narrow Angle Camera (NAC) scattered-light images (PSR ID SP_809710_0357350) (Figures 1b and 1c), and previous predictions that this crater contains regions where both surface ice and subsurface ice should be thermally stable (Paige et al., 2010; Pugacheva et al., 2018). Analyses of orbital UV, infrared and neutron data (Fisher et al., 2017; Hayne et al., 2015; Li et al., 2018; Sanin et al., 2017) thus far have not indicated the presence of either surface or subsurface ice in Scott-E crater.
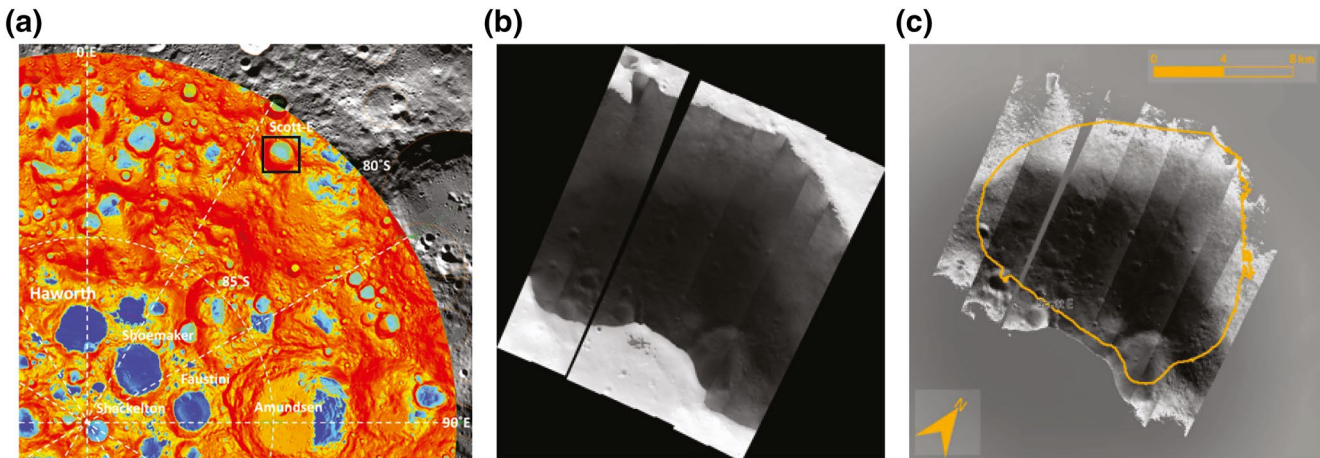
**Figure 1.** (**a**) Location of Scott-E crater shown in the black box. Color basemap is summer maximum temperatures from Diviner measurements (Williams et al., 2017). Monochrome basemap is global mosaic from LROC Wide Angle Camera image. (b) LROC NAC mosaic of a portion of Scott-E crater acquired near noon local time. The image brightness is stretched to reveal detail in both the illuminated and shadowed regions. Mosaic resolution is ∼5 m/pixel. (c) LROC PSR Atlas image of Scott-E crater from Cisneros et al. (2018). The yellow polygon in (c) shows the approximate boundary of the crater's permanently shadowed region. LROC, Lunar Reconnaissance Orbiter Camera; NAC, Narrow Angle Camera; PSR, permanently shadowed region.

### 2.2. Quantification of Surface Roughness

Surface roughness quantifies surface elevation changes and is commonly used in studies of planetary and terrestrial environments (Kreslavsky & Head, 2000; Li et al., 2018; Rosenburg et al., 2011). There are various mathematical and statistical methods to calculate surface roughness, such as the interquartile range of curvature (the second derivative of elevation) (Kokhanov et al., 2019), median differential slope (Kreslavsky & Head, 2000), or the standard deviation of elevation gradients (Frankel & Dolan, 2007). Most methods aim to effectively capture spatial variations of surface elevation (Smith, 2014).

In this study, we quantify the spatial distribution of roughness using two data sets: LOLA altimetry and LROC-NAC images. First, we quantify surface roughness using a 1,024 pixel per degree (ppd) digital elevation model (DEM) from the LOLA (Smith et al., 2010). The raw DEM is projected into a south-polar stereographic projection with a resolution of 20 m/pixel. The LOLA DEM has numerical artifacts associated with track lines (apparent in Figures 2a and 2d). To reduce the influences of artifacts on geomorphic analysis, we average the elevation within a 100 m-radius circular window, which is ∼8 times larger than the spacing of original laser shot measurements (∼25 m) and ∼3.3 times the width of one measurement's quintuple-laser surface footprint (∼60 m), respectively. Then, we calculate the elevation gradient (dimensionless) in the direction of the steepest descent considering eight neighboring 20-m pixels. Surface roughness is calculated as the standard deviation of elevation gradients among eight neighboring cells, following Frankel and Dolan (2007). Hereafter, roughness calculated using the LOLA DEM is referred to as elevation-derived roughness (dimensionless).

Second, we calculate surface roughness using images from LROC NAC. Due to the inherent darkness of PSRs, these particular images rely on sunlight scattered off of surrounding surfaces to indirectly illuminate shadowed crater-interior surfaces. The four images covering Scott-E crater used here were acquired at ∼0.9 m/pixel across track and ∼9.9 m/pixel along track on consecutive orbits near local noon in September 2013 (M1134048259L&R, M1134026938L&R, M1134034045L&R, M1134041152L&R, as listed in the LROC PSR Atlas [Cisneros et al., 2018]) (Figures 1b and 1c). Raw images are calibrated, projected, and mosaicked in USGS ISIS software (to south-polar stereographic projection, 5 m/pixel). Pixel values of the entire four-image mosaic in I/F units range from −0.000127 to 0.0492. Illuminated portions of the crater rim are not quantitatively considered in this study, so the pixel range is constrained to −0.0001 to 0.0016 (I/F units) before linearly scaling and exporting to a 10-bit TIFF image (DN range 0–65,535). Hereafter, all calculations are done on this TIFF image in DN units.

The LROC image mosaic also has numerical artifacts associated with track lines (Figures 2b, 2e, 2g, and 2h). To reduce effects from artifacts, we calculate average brightness within a 25 m-radius circular window,
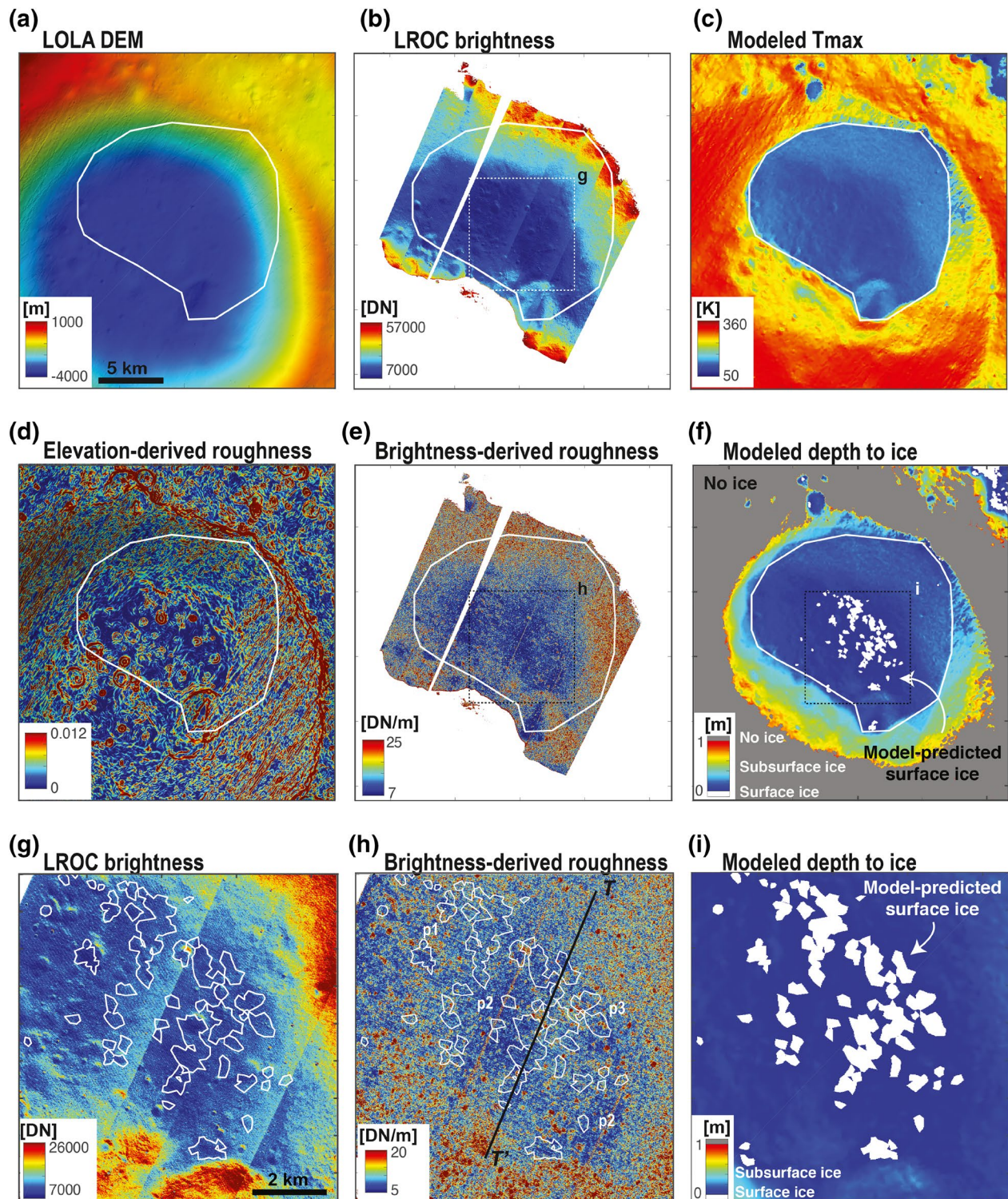
**Figure 2.** Maps of Scott-E crater showing (a–f) northeastern wall and floor and (g-i) close-up of the crater floor within a permanently shadowed region (PSR). (a) LOLA Digital Elevation Model (DEM) with a resolution of ∼ 20 m (Smith et al., 2010), (b and g) LROC brightness with stretched DN values (DN), (c) modeled annual maximum temperature (Tmax), (d) elevation-derived roughness. (e and h) brightness-derived roughness, (f and i) modeled depth to thermally stable water ice. White polygon in (a–f) and (g–h) shows the PSR boundary from Cisneros et al. (2018) and the areas with model predicted surface ice, respectively. The transect T-T' for Figure S3 is shown as a black line in (h). The calculated roughnesses from elevation and brightness show an overall correspondence, suggesting that roughness calculated from brightness can also be used to characterize surface texture. The roughness values significantly decrease where stable surface ice is predicted in thermal models. LOLA, Lunar Orbiter Laser Altimeter; LROC, Lunar Reconnaissance Orbiter Camera; PSR, permanently shadowed region.

which is ∼50 and ∼10 times larger than the resolution of the raw image and projected mosaic, respectively. Then, we calculate the brightness gradient (DN/m) in the direction of steepest descent considering eight neighboring cells. We calculate roughness as the standard deviation of the brightness gradients among eight neighboring cells, similar to Frankel and Dolan (2007). Hereafter, roughness calculated from LROC images is referred to as the brightness-derived roughness (DN/m). Both elevation-derived and brightness-derived roughnesses are calculated using MATLAB Topotoolbox 2 (Schwanghart & Scherler, 2014). In summary, elevation-derived roughness will effectively capture the variations in elevation gradients over ∼200 m scale, and the brightness-derived roughness will effectively capture changes in brightness gradients over ∼50 m scale.

### 2.3. Thermal State and Surface Ice Stability

To infer the thermal state and surface-ice stability over Scott-E crater, we use a thermal model developed in previous studies (Paige et al., 2010, 2013; Siegler et al., 2011, 2016; Siegler and Smrekar, 2014). The model calculates the scattered and reflected sunlight and re-radiated thermal emission from all surfaces, which is critical to estimating temperatures within shadowed craters. By tracking the temporal variations of maximum temperature with depth over multiple years, the model predicts the location and depth of thermally stable ice deposits within the regolith. The results of this model are in good agreement with Diviner thermal emission measurements in the Moon's PSRs (Paige et al., 2010) and with the boundaries of radar-bright ice deposits on Mercury (Paige et al., 2013). As the regolith itself is only estimated to be 10–15 m thick, thermal models at this scale will provide information on the possible presence of ice that could alter the physical properties of regolith.

We use this thermal model to calculate thermal quantities of the regolith within Scott-E crater and the surrounding region, which is represented by a ∼118 m/pixel south-polar stereographic projection of a 128 ppd LOLA DEM. The DEM obtained from the LOLA PDS archive was triangulated and then reduced in complexity to 27% of its original triangle count using a fast quartic mesh simplification algorithm (Garland & Heckbert, 1997). Although other higher-resolution DEM products do exist, the use of a lower-resolution DEM is required to reduce slope artifacts that can cause errors in the thermal model. The thermal model calculates quantities including annual minimum, maximum, and average temperatures as a function of depth, as well as the depth to thermally stable water ice including the effects of subsurface water diffusion through overlying regolith layers at a loss rate of 1 mm/Gyr (Paige et al., 2010). The thermal model results are resampled at 5 m/pixel using a linear interpolation for comparison with brightness-derived roughness. Additionally, a comparison of the native-resolution (∼118 m/pixel) thermal model to significantly reduced-resolution (∼120 m/pixel) brightness-derived roughness results is presented in Supplementary Information (Figures S1 and S2).

## 3. Results and Discussion

### 3.1. Surface Roughness Variation within Scott-E Crater

Examination of the NAC image mosaic reveals large-scale spatial variations in brightness across the entire crater due to variations in the illumination of the crater wall and floor by scattered sunlight (Figure 2b). Similarly to previous studies (Koeber & Robinson, 2013; Sargeant et al., 2020), brightness values show no obvious change across the permanent-shadow boundary. This finding indicates either that there may not be bright surface volatile deposits or other compositional changes across the permanent shadow boundary, or that the broad-band wavelength channel of LROC NAC may fail to detect existing changes. However, the LROC images reveal numerous, small, 10s–100s meter-scale variations in brightness within the permanent shadow boundary, likely associated with small-scale topographic or surface texture variations (Figures 2e and 2h).

The brightness-derived roughness allows us to examine the spatial patterns of brightness variability. While elevation-derived roughness is a dimensionless quantity, the absolute value of brightness-derived roughness has a unit of DN/m. The absolute values of brightness-derived roughness are influenced by the illumination level and resolution of original optical images, the method of stretching the original DN values,

and the length scale for calculating brightness gradients. This makes it difficult to directly compare the absolute values of brightness-derived roughnesses from two different images or two distant areas within one image. Brightness-derived roughness will allow us to examine spatial patterns of surface variations within proximal areas of similar brightness levels. However, we need to be cautious because an absence of differences in brightness-derived roughness in different areas may not necessarily mean there are no differences in surface texture or relief between those areas. For very high (saturated) or very low (undetectable) surface-brightness levels, topographic or surface texture variations may not produce any measurable differences in brightness-derived roughness. However, if there are any measurable differences in brightness-derived roughness, they are likely derived from topographic or surface texture variations.

Our analysis of brightness-derived roughness produces several potentially interesting results. First, brightness-derived roughness (Figure 2e) shows similar overall patterns with elevation-derived roughness (Figure 2d). Higher roughness values are observed on the walls of Scott-E crater, while lower roughness is observed on the bottom of the crater. Although we do not know exactly what causes the differences in roughness, we speculate that they could be due to the differences in surface processes or materials on slopes. Overall correspondence between brightness-derived roughness and elevation-derived roughness confirms that changes of brightness in LROC images can also be used to capture variations of surface textures, similar to that derived from changes of surface elevation from LOLA (Figures 2d and 2e). Second, the brightness-derived roughness shows more spatial variability than elevation-derived roughness due to the higher resolution of the projected LROC images compared to the projected LOLA DEM (Figures 2d and 2e). Lastly, although brightness-derived roughness is lower in areas with lower brightness DN values, there are large variations of roughness in relatively wide ranges of brightness DN values (Figures 2b, 2e, 2g, 2h, and 3a, 3d). Within areas of low brightness, both high and low brightness-derived roughness values exist and often occur close to each other. This result suggests that there are factors other than scattered-light illumination levels that induce the variations of brightness-derived roughness observed, which causes the roughness to deviate from the overall trend of brightness DN values.

### 3.2. Thermal Model Results

The results of the thermal model show that more than half of the crater is shadowed from diurnal illumination at any given time, and roughly one-third of the floor of Scott-E crater remains in permanent shadow. In the outer permanently shadowed areas, maximum annual temperatures remain below 250 K, with average temperatures below 80 K (Figure 2c). These areas could retain ice within the upper meter of the lunar regolith, potentially affecting regolith physical properties. At the core of the permanently shadowed region, annual maximum temperatures remain below 100 K, which implies the possible presence of thermally stable water ice on the surface as well as below the surface (Figures 2f and 2i).

### 3.3. Comparison Between Surface Roughness and Modeled Regolith Properties

Comparing the brightness-derived roughness, modeled annual maximum temperature (Tmax), and predicted depth of ice reveal additional interesting patterns (Figures 2 and 3). First, the measured ranges of brightness-derived roughness differ in areas with model-predicted surface ice, subsurface ice, and no ice (Figures 2e, 2f, 2h, 2i, and 3c, 3f, 3i). The brightness-derived roughness in the region where surface ice would be stable is significantly lower than that in areas with predicted subsurface ice or no ice (Figures 2e and 2f). Considering the different data sources of the thermal model (LOLA DEM) and roughness calculation (LROC brightness), the spatial correspondence between observed low surface roughness and model-predicted surface ice is intriguing (Figure 2h and Figure S3).

Second, although we observe an overall correspondence between low brightness-derived roughness and modeled stable surface ice, local deviations exist. When we examine a close-up location of the crater floor (Figures 2g–2i), the correspondence is clear both along a transect (T-T' in Figure S3) and over a delineated area in the northwestern crater floor (p1 in Figure 2h). However, in some locations (p2 in Figure 2h), low roughness areas exist without modeled stable surface ice. In other locations (p3 in Figure 2h), there are high
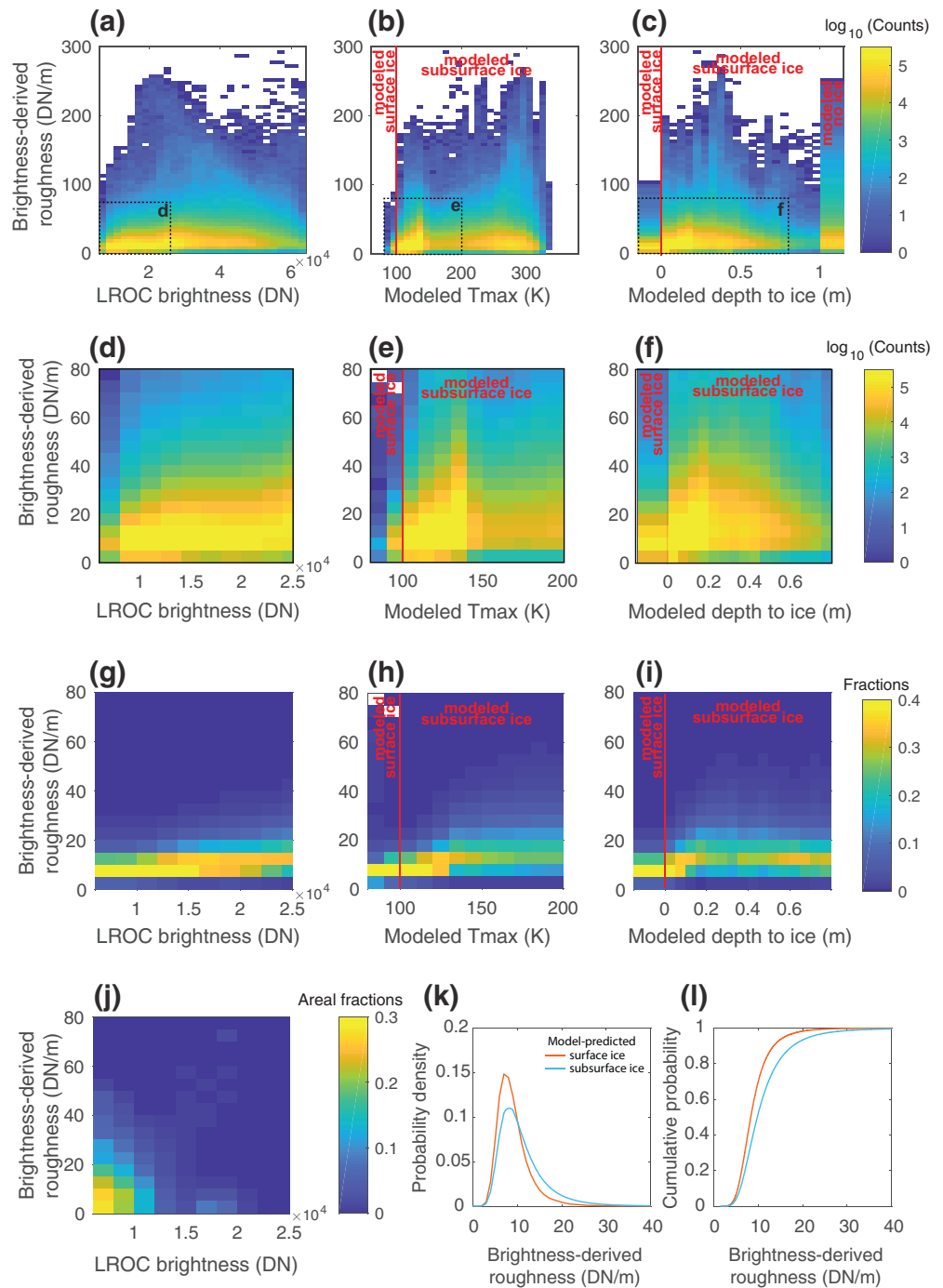
**Figure 3.** Heat maps showing relationships between brightness-derived roughness and (a, d, g, j) LROC brightness (DN), (b, e, h) modeled Tmax, and (c, f, i) modeled depth to thermally stable water ice. The ranges of axes in (a–c) differ from those in (d–j). The dotted boxes in (a–c) show the ranges of axes shown in (d–j). The color in (a–f), (g–i), and (j) indicates the total number of data points in log scale, the fraction of data points within the bin in the x-axis, and the fraction of area where stable surface ice is predicted in thermal models within the bin in x and y-axes, respectively. A warmer color represents a higher density of data points or a higher fraction for a given range. Red lines in (b–c, e–f, and h–i) separate the regimes where the thermal model predicts stable surface water ice, subsurface water ice, or no water ice. The line plots show (k) probability and (l) cumulative probability distributions of brightness-derived roughness from areas where thermally stable surface ice (orange) or subsurface ice (light-blue) are predicted in thermal models. The areas with the LROC brightness (DN) less than $1.7 \times 10^4$, which include 95% of thermally stable surface ice, are considered. Areas with thermally stable surface ice tend to have lower roughness values compared to areas with subsurface ice or no ice. LROC, Lunar Reconnaissance Orbiter Camera.

roughness peaks in the areas with predicted modeled stable surface ice. Such local variations can result from processes not related to thermal effects, such as impact cratering.

Third, brightness-derived roughness tends to be lower in floor regions with lower brightness values (Figures 2b, 2e and 3a, 3d). However, within these low-brightness areas, subareas with a higher areal fraction of predicted surface ice (Figures 2g–2i) tend to have lower brightness-derived roughness (Figure 3j). Although the absolute areal fraction of predicted surface ice shows a decreasing trend with increasing surface brightness, the correlation of higher relative areal fractions of predicted surface ice and lower brightness-derived roughness values holds over a wide range of surface brightness. Ninety-five percent of thermally stable surface ice occurs in areas with surface brightness $<1.7 \times 10^4$ DN. We compare the cumulative probability distribution (CPD) of brightness-derived roughness from areas with predicted surface ice with that from areas with predicted subsurface ice, all within this area of low surface brightness. These CPDs of brightness-derived roughness from the two areas are significantly different, according to the Kolmogorov-Smirnov test ($p < 0.05$) (Figures 3k and 3l, Supplementary Information). We obtain consistent results from the same comparison preformed on images resampled at ~120 m/pixel, similar to the resolution of thermal models (Supplementary Information; Figures S1 and S2). Our analysis indicates that high roughness values likely disappear with the modeled possible existence of surface ice.

Fourth, surface roughness shows distinctive changes across the boundary between areas of surface ice and areas of subsurface ice or no ice stability (Figures 3c, 3f, and 3i). The fractional distributions of brightness-derived roughness are similar for areas with a modeled depth to ice of >0.1 m (Figure 3i). These distributions are different from those in areas with predicted surface ice. This difference may represent a transition from surface ice to near-surface ice within the upper ~0.1 m, which may be related to the involvement of near-surface ice in surface processes. Alternatively, the difference may reflect uncertainties stemming from different resolutions of the thermal model and image data.

By characterizing the spatial variation of brightness-derived roughness using LROC NAC images, we quantify the variation in surface texture at spatial scales over 10s–100s of meters within the entire shadowed region. Considering overall slope gradients in this area are 0.01–0.1 (measured from a DEM averaged over a 100 m-radius circular window from the 20 m/pixel LOLA DEM [Figure 2a]), this 10s–100s meter-scale roughness likely reflects submeter-to meter-scale amplitude variability of topographic features. The length scales of topographic amplitude changes may be due either to the depth of ice deposits or to transport processes affected by thermally stable surface ices. Interestingly, the submeter-to meter-scales of topographic variations are similar to the scales of anticipated depths of suspected ice deposits from previous studies (Campbell et al., 2003; Qiao et al., 2019).

## 3.4. Potential Mechanisms for Surface Roughness and the Presence of Surface Ice

By combining geomorphic analysis and thermal model results, we find that areas predicted to have the coldest temperatures and surface ice stability have more subdued surface roughness values than those predicted to have subsurface ice or no ice. We suggest three plausible mechanisms that can produce the observed connections between surface roughness and thermal model results.

First, hillslope transport of lower density material leads to more subdued topographic roughness in areas with surface or near-surface water ice or volatiles. The hillslope evolution model of diffusive processes like creep shows that changes in elevation with time depend on both topographic curvature and the diffusion coefficient, which is inversely related to bulk density of the surface material (Culling, 1960; Fernandes & Dietrich, 1997). The existence of water ice or volatiles on the surface or within regolith may result in surface material with lower densities compared to ice-free regolith. When transport of regolith is induced by gravity or surface disturbances from primary impacts or secondary ejectors (Chamberlain & Boynton, 2007; Mustard et al., 2001), regolith material with ice or volatiles will fill depressed areas more efficiently and evolve toward more subdued topography.

Second, cold trapping of ice may preferentially occur in areas with depressions (e.g., small craters) or high albedos within PSRs (Prem et al., 2018; Watson et al., 1961). In particular, areas doubly shadowed from reflected visible and re-radiated infrared radiation tend to have lower temperatures than surrounding regions

(Paige et al., 2010; Williams et al., 2017). If water is available, preferential trapping of water ice or volatiles in depressions may lead to the smoothing of surfaces (Deutsch et al., 2020; Prem et al., 2018). Similarly, if cold-trapping occurs preferentially in high albedo areas, this can lead to subdued brightness-derived roughness. Interestingly, a recent study finds that the interiors of small permanently shadowed craters (diameters < 15 km) with ice detected by the $M^3$ instrument tend to have lower average roughness values than those without ice (Deutsch et al., 2020). Analogous processes and the existence of cold trapping of ice and volatiles have been proposed as causes for the thermal segregation of water ice on Mercury and the Galilean Satellites (Deutsch et al., 2017; Spencer, 1987).

Third, physical properties of surface materials (e.g., fluffiness, frost, and grain size) may be influenced by variations in temperature and affect the reflectance of the surface. If brightness-derived roughness calculations are heavily influenced by spatial variations in scattered-light illumination or surface reflectance, as opposed to relief, low brightness-derived roughness values may also be expected in areas of low temperature without predicted ice. However, we observe overall consistent distributions of brightness-derived roughness based on LROC images and elevation-derived roughness based on topographic data (Figure 2). In addition, there are large variations in brightness-derived roughness, which cannot be simply explained by the brightness levels (Figure 3j). Thus, we suggest that the observed, subdued surface roughness in areas with predicted surface ice is likely due to relatively increased transport efficiency or cold trapping potential, rather than differences in surface reflectance or illumination.

## 4. Conclusions

We have investigated the connections between geomorphic characteristics of landforms and the thermal state of lunar regolith in permanently shadowed regions of Scott-E crater in the south polar region of the Moon. We characterized surface roughness based on the high-resolution digital elevation model from LOLA and based on scattered-light images from LROC NAC. We modeled the thermal quantities of lunar regolith and the stability of surface and subsurface ice within the crater. Comparing these results reveals that surface roughness does not vary significantly across PSR boundaries but does show large differences depending on the modeled potential presence of surface ice. The brightness-derived roughness in areas with high potential for the presence of surface ice is more subdued than that found in areas of modeled subsurface ice or no ice. This correspondence indicates that the presence of surface ice deposits on the Moon may leave detectable changes in surface relief or texture. The potential mechanisms that cause these topographic signatures include enhanced ice-rich regolith transport due to the presence of ice and preferential ice trapping in depressions. Our study utilizes quantitative methods of both geomorphic analysis and thermal modeling. Although there is no direct evidence of the detected ice in Scott-E according to remote-sensing data, we find a potential connection between brightness-derived roughness and modeled surface ice. High-resolution topography and multiple low-illumination images from future missions (e.g., ShadowCam in the Korean Pathfinder Lunar Orbiter mission) coupled with thermal models may help to document surface-roughness patterns in other PSR craters that are consistent with those in Scott-E. Future studies based on these data sets may further establish the connections between surface roughness and surface and subsurface ice and help to identify the dominant mechanism.

## Data Availability Statement

LOLA DEM and LROC NAC images used in this study were accessed from the LOLA PDS data node (http://imbrium.mit.edu/) and the LROC PDS archive (http://lroc.sese.asu.edu/archive). Surface roughness and thermal model results for Scott-E are available at http://doi.org/10.5281/zenodo.4050849.

## References

Boeckli, L., Brenning, A., Gruber, S., & Noetzli, J. (2012). Permafrost distribution in the European Alps: Calculation and evaluation of an index map and summary statistics. *The Cryosphere*, 6(4), 807–820.

Calef, F. J., Arvidson, R., Sletten, R., Williams, R., & Grotzinger, J. (2014). *Surface roughness derived from HIRISE visible imagery: A case study at the MSL landing site*. Paper presented at 45th Lunar and Planetary Science Conference, Woodlands, TX.

Campbell, B. A., Campbell, D. B., Chandler, J. F., Hine, A. A., Nolan, M. C., & Perillat, P. J. (2003). Radar imaging of the lunar poles. *Nature*, *426*(6963), 137–138. https://doi.org/10.1038/426137a

Chabot, N. L., Ernst, C. M., Paige, D. A., Nair, H., Denevi, B. W., Blewett, D. T., et al. (2016). Imaging Mercury's polar deposits during MESSENGER'S low-altitude campaign. *Geophysical Research Letters*, *43*(18), 9461–9468. https://doi.org/10.1002/2016GL070403

Chamberlain, M. A., & Boynton, W. V. (2007). Response of Martian ground ice to orbit-induced climate change. *Journal of Geophysical Research*, *112*(E6), E06009. https://doi.org/10.1029/2006je002801

Cisneros, E., Boyd, A., Brown, H., Awumah, A., Martin, A., Paris, K., et al. (2018). *Lunar reconnaissance orbiter camera: Permanently shadowed regions atlas*. https://www.lroc.asu.edu/psr

Colaprete, A., Schultz, P., Heldmann, J., Wooden, D., Shirley, M., Ennico, K., et al. (2010). Detection of water in the LCROSS ejecta plume. *Science*, *330*(6003), 463–468. https://doi.org/10.1126/science.1186986

Culling, W. E. H. (1960). Analytical theory of erosion. *The Journal of Geology*, *68*(3), 336–344.

Deutsch, A. N., Head, J. W., Neumann, G. A., Kreslavsky, M. A., & Barker, M. K. (2020). Assessing the roughness properties of circumpolar lunar craters: Implications for the timing of water-ice delivery to the moon. *Geophysical Research Letters*, *47*(15), e2020GL087782. https://doi.org/10.1029/2020gl087782

Deutsch, A. N., Neumann, G. A., & Head, J. W. (2017). New evidence for surface water ice in small-scale cold traps and in three large craters at the north polar region of Mercury from the Mercury Laser Altimeter. *Geophysical Research Letters*, *44*(18), 9233–9241. https://doi.org/10.1002/2017GL074723

Fernandes, N. F., & Dietrich, W. E. (1997). Hillslope evolution by diffusive processes: The timescale for equilibrium adjustments. *Water Resources Research*, *33*(6), 1307–1318. https://doi.org/10.1029/97wr00534

Fisher, E. A., Lucey, P. G., Lemelin, M., Greenhagen, B. T., Siegler, M. A., Mazarico, E., et al. (2017). Evidence for surface water ice in the lunar polar regions using reflectance measurements from the Lunar Orbiter Laser Altimeter and temperature measurements from the Diviner Lunar Radiometer Experiment. *Icarus*, *292*, 74–85. https://doi.org/10.1016/j.icarus.2017.03.023

Fortezzo, C., Spudis, P., & Harrel, S. (2020). *Release of the digital unified global geologic map of the Moon at 1: 5,000,000-Scale*. Paper presented at 51st Lunar and Planetary Science Conference, Lunar and Planetary Institute, Houston, TX.

Frankel, K. L., & Dolan, J. F. (2007). Characterizing arid region alluvial fan surface roughness with airborne laser swath mapping digital topographic data. *Journal of Geophysical Research*, *112*(F2). https://doi.org/10.1029/2006jf000644

Garland, M., & Heckbert, P. S. (1997). Surface simplification using quadric error metrics. In *Proceedings of the 24th Annual Conference on Computer Graphics and Interactive Techniques* (pp. 209–216). https://doi.org/10.1145/258734.258849

Harmon, J. K. (2008) Radar imaging of Mercury. In A. Balogh, L. Ksanfomality, & R. von Steiger (Eds.), Mercury. Space Sciences Series of ISSI (Vol. 26, pp. 125–167). New York, NY: Springer. https://doi.org/10.1007/978-0-387-77539-5_7

Hayne, P. O., Hendrix, A., Sefton-Nash, E., Siegler, M. A., Lucey, P. G., Retherford, K. D., et al. (2015). Evidence for exposed water ice in the Moon's south polar regions from Lunar Reconnaissance Orbiter ultraviolet albedo and temperature measurements. *Icarus*, *255*, 58–69. https://doi.org/10.1016/j.icarus.2015.03.032

Kim, J. R., & Muller, J. P. (2008). Very high resolution stereo DTM extraction and its application to surface roughness estimation over Martian surface. *International Archives of the Photogrammetry, Remote Sensing and Spatial Information Sciences*, *37*(B4), 993–998.

Koeber, S., & Robinson, M. (2013). *LROC observations of permanently shadowed regions*. Paper presented at 44th Lunar and Planetary Science Conference, Woodlands, TX.

Kokhanov, A. A., Karachevtseva, I. P., & Zharkova, A. (2019). Topographic roughness as interquartile range of the second derivatives: Calculation and mapping. In H. Hargitai (Ed.), *Planetary Cartography and GIS. Lecture Notes in Geoinformation and Cartography* (pp. 315–324). Cham, Switzerland: Springer. https://doi.org/10.1007/978-3-319-62849-3_18

Kreslavsky, M. A., & Head, J. W. (2000). Kilometer-scale roughness of Mars: Results from MOLA data analysis. *Journal of Geophysical Research*, *105*(E11), 26695–26711. https://doi.org/10.1029/2000je001259

Kreslavsky, M. A., Head, J. W., Neumann, G. A., Rosenburg, M. A., Aharonson, O., Smith, D. E., & Zuber, M. T. (2013). Lunar topographic roughness maps from Lunar Orbiter Laser Altimeter (LOLA) data: Scale dependence and correlation with geologic features and units. *Icarus*, *226*(1), 52–66. https://doi.org/10.1016/j.icarus.2013.04.027

Lawrence, D. J. (2017). A tale of two poles: Toward understanding the presence, distribution, and origin of volatiles at the polar regions of the Moon and Mercury. *Journal of Geophysical Research: Planets*, *122*(1), 21–52. https://doi.org/10.1002/2016je005167

Li, S., Lucey, P. G., Milliken, R. E., Hayne, P. O., Fisher, E., Williams, J.-P., et al. (2018). Direct evidence of surface exposed water ice in the lunar polar regions. *Proceedings of the National Academy of Sciences*, *115*(36), 8907–8912. https://doi.org/10.1073/pnas.1802345115

Mahaney, W. C., Miyamoto, H., Dohm, J. M., Baker, V. R., Cabrol, N. A., Grin, E. A., & Berman, D. C. (2007). Rock glaciers on Mars: Earth-based clues to Mars' recent paleoclimatic history. *Planetary and Space Science*, *55*(1), 181–192. https://doi.org/10.1016/j.pss.2006.04.016

Mangold, N. (2003). Geomorphic analysis of lobate debris aprons on Mars at Mars Orbiter Camera scale: Evidence for ice sublimation initiated by fractures. *Journal of Geophysical Research*, *108*(E4). https://doi.org/10.1029/2002je001885

Mustard, J. F., Cooper, C. D., & Rifkin, M. K. (2001). Evidence for recent climate change on Mars from the identification of youthful near-surface ground ice. *Nature*, *412*(6845), 411–414. https://doi.org/10.1038/35086515

Paige, D. A., Siegler, M. A., Zhang, J., Hayne, P. O., Greenhagen, B. T., Foote, E. J., et al. (2010). Diviner Lunar Radiometer observations of cold traps in the Moon's south polar region. *Science*, *330*(6003), 479–482. https://doi.org/10.1126/science.1187726

Paige, D. A., Siegler, M. A., Harmon, J. K., Neumann, G. A., Mazarico, E. M., Smith, D. E., et al. (2013). Thermal stability of volatiles in the north polar region of Mercury. *Science*, *339*(6117), 300–303. https://doi.org/10.1126/science.1231106

Prem, P., Goldstein, D. B., Varghese, P. L., & Trafton, L. M. (2018). The influence of surface roughness on volatile transport on the Moon. *Icarus*, *299*, 31–45. https://doi.org/10.1016/j.icarus.2017.07.010

Pugacheva, S. G., Feoktistova, E. A., & Shevchenko, V. V. (2018). On the possibility of the existence of volatile compounds in the region of the Scott crater on the Moon. *Cosmic Research*, *56*(3), 169–179.

Qiao, L., Ling, Z., Head, J. W., Ivanov, M. A., & Liu, B. (2019). Analyses of lunar orbiter laser altimeter 1,064-nm albedo in permanently shadowed regions of polar crater flat floors: Implications for surface water ice occurrence and future in situ exploration. *Earth and Space Science*, *6*(3), 467–488. https://doi.org/10.1029/2019ea000567

Rosenburg, M. A., Aharonson, O., Head, J. W., Kreslavsky, M. A., Mazarico, E., Neumann, G. A., et al. (2011). Global surface slopes and roughness of the Moon from the lunar orbiter laser altimeter. *Journal of Geophysical Research*, *116*(E2). https://doi.org/10.1029/2010je003716

Rossbacher, L. A., & Judson, S. (1981). Ground ice on Mars: Inventory, distribution, and resulting landforms. *Icarus*, *45*(1), 39–59. https://doi.org/10.1016/0019-1035(81)90005-1

Rubanenko, L., Venkatraman, J., & Paige, D. A. (2019). Thick ice deposits in shallow simple craters on the Moon and Mercury. *Nature Geoscience*, *12*(8), 597–601.

Salamunićcar, G., Lončarić, S., Grumpe, A., & Wöhler, C. (2014). Hybrid method for crater detection based on topography reconstruction from optical images and the new LU78287GT catalogue of Lunar impact craters. *Advances in Space Research*, *53*(12), 1783–1797. https://doi.org/10.1016/j.asr.2013.06.024

Sanin, A., Mitrofanov, I., Litvak, M., Bakhtin, B., Bodnarik, J., Boynton, W. V., et al. (2017). Hydrogen distribution in the lunar polar regions. *Icarus*, *283*, 20–30.

Sargeant, H. M., Bickel, V. T., Honniball, C. I., Martinez, S. N., Rogaski, A., Bell, S. K., et al. (2020). Using boulder tracks as a tool to understand the bearing capacity of permanently shadowed regions of the Moon. *Journal of Geophysical Research: Planets*, *125*(2), e2019JE006157. https://doi.org/10.1029/2019je006157

Schwanghart, W., & Scherler, D. (2014). Short communication: TopoToolbox 2 – MATLAB-based software for topographic analysis and modeling in Earth surface sciences. *Earth Surface Dynamics*, *2*(1), 1–7. https://doi.org/10.5194/esurf-2-1-2014

Siegler, M. A., Bills, B. G., & Paige, D. A. (2011). Effects of orbital evolution on lunar ice stability. *Journal of Geophysical Research*, *116*(E3), 159. https://doi.org/10.1029/2010JE003652

Siegler, M. A., Miller, R. S., Keane, J. T., Laneuville, M., Paige, D. A., Matsuyama, I., et al. (2016). Lunar true polar wander inferred from polar hydrogen. *Nature*, *531*(7595), 480–484. https://doi.org/10.1038/nature17166

Siegler, M., & Smrekar, S. (2014). Lunar heat flow: Regional prospective of the Apollo landing sites. *Journal of Geophysical Research: Planets*, *119*(1), 47–63. https://doi.org/10.1002/2013JE004453

Smith, M. W. (2014). Roughness in the Earth sciences. *Earth-Science Reviews*, *136*, 202–225. https://doi.org/10.1016/j.earscirev.2014.05.016

Smith, D. E., Zuber, M. T., Jackson, G. B., Cavanaugh, J. F., Neumann, G. A., Riris, H., et al. (2010). The lunar orbiter laser altimeter investigation on the lunar reconnaissance orbiter mission. *Space Science Reviews*, *150*(1), 209–241. https://doi.org/10.1007/s11214-009-9512-y

Spencer, J. R. (1987). Thermal segregation of water ice on the Galilean satellites. *Icarus*, *69*(2), 297–313. https://doi.org/10.1016/0019-1035(87)90107-2

Squyres, S. W., & Carr, M. H. (1986). Geomorphic evidence for the distribution of ground ice on Mars. *Science*, *231*(4735), 249–252. https://doi.org/10.1126/science.231.4735.249

Watson, K., Murray, B. C., & Brown, H. (1961). The behavior of volatiles on the lunar surface. *Journal of Geophysical Research*, *66*(9), 3033–3045. https://doi.org/10.1029/JZ066i009p03033

Williams, J. P., Williams, J. P., Paige, D. A., Greenhagen, B. T., & Sefton-Nash, E. (2017). The global surface temperatures of the Moon as measured by the diviner lunar radiometer experiment. *Icarus*, *283*, 300–325. https://doi.org/10.1016/j.icarus.2016.08.012

Zuber, M. T., Head, J. W., Smith, D. E., Neumann, G. A., Mazarico, E., Torrence, M. H., et al. (2012). Constraints on the volatile distribution within Shackleton crater at the lunar south pole. *Nature*, *486*(7403), 378–381. https://doi.org/10.1038/nature11216